

# Structural Implications of the Paramagnetically Shifted NMR Signals from Pyridine H-Atoms on Synthetic Nonheme Fe<sup>IV</sup>=O Complexes

Waqas Rasheed,<sup>a</sup> Ruixi Fan,<sup>b</sup> Chase S. Abelson,<sup>a</sup> Paul O. Peterson,<sup>a</sup> Wei-Min Ching,<sup>a</sup> Yisong Guo,<sup>\*,b</sup> and Lawrence Que, Jr.<sup>\*,a</sup>

Department of Chemistry and Center of Metals in Biocatalysis, University of Minnesota – Twin Cities, 207 Pleasant Street SE, Minneapolis, Minnesota 55455, United States

Department of Chemistry, Carnegie Mellon University, Pittsburgh, PA 15213, United States

Keywords: nonheme iron, iron(IV)-oxo complexes, NMR

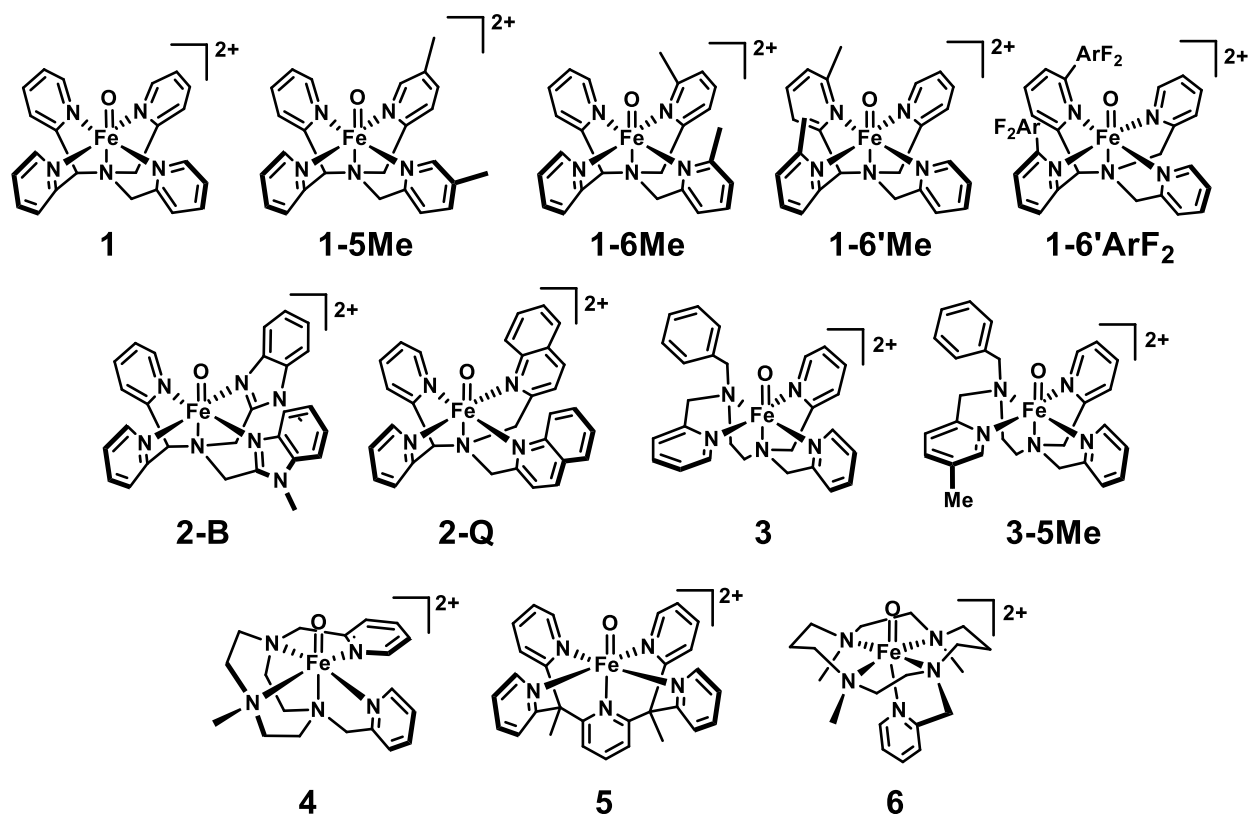
---

**Abstract:** Oxoiron(IV) motifs are found in important intermediates in many enzymatic cycles that involve oxidations. Over half of the reported synthetic nonheme oxoiron(IV) analogs incorporate heterocyclic donors, with a majority of them comprising pyridines. Herein we report an <sup>1</sup>H-NMR study of oxoiron(IV) complexes containing pyridines that are arranged in different configurations relative to the Fe=O unit and give rise to paramagnetically shifted resonances that differ by as much as 50 ppm. The strong dependence of <sup>1</sup>H-NMR shifts on the different configurations and orientation of pyridines relative to the oxoiron(IV) unit demonstrates how unpaired electronic spin density of the iron center affects the chemical shifts of these protons.

---

Oxoiron(IV) intermediates involved in oxygen activation have been trapped as reactive species in many mononuclear nonheme iron enzymes.<sup>1-6</sup> In attempts to model these intermediates, bioinorganic chemists have to date identified over 90 nonheme iron oxoiron(IV) complexes supported by various polydentate ligand frameworks, and crystal structures of thirteen of these complexes have been solved.<sup>7-9</sup> Most of these crystallographically characterized complexes are supported by ligands based on the macrocyclic TMC (six, TMC = 1,4,8,11-tetramethyl-1,4,8,11-tetraazacyclotetradecane)<sup>10-14</sup> framework or on the pentadentate N4Py (four, N4Py = 1,1-di(pyridin-2-yl)-*N,N*-bis(pyridin-2-ylmethyl)-methanamine) ligand and its variants.<sup>15-17</sup> These structures provide a reservoir of information with which to understand the spectroscopic and reactivity properties of the Fe<sup>IV</sup>=O unit.

<sup>1</sup>H-NMR spectroscopy is a potentially useful probe of the electronic structures and geometries of paramagnetic complexes<sup>18-19</sup> but has not been applied extensively to investigation of this interesting family of complexes, except for a few reports. In 2005, Klinker *et al.* reported the first use of <sup>1</sup>H-NMR spectroscopy to characterize the nonheme oxoiron(IV) complex [Fe<sup>IV</sup>(O)(N4Py)]<sup>2+</sup> (**1**).<sup>15</sup> N4Py is a pentadentate N5 ligand based on a tertiary amine to which are connected two 2-pyridylmethyl arms that provide a pair of pyridine donors and a bis(2-pyridyl)methyl arm that provides a second pair of pyridine donors. Together, these pyridines can bind to an Fe=O unit to form a 4-pyridine equatorial plane with the tertiary amine trans to the oxo atom. The crystal structure of **1**, in fact, confirms this expected binding configuration, and the two pyridines in each pair are related to each other by a mirror plane of symmetry. Over half of the oxoiron(IV) complexes reported since then incorporate heterocycles into their ligand frameworks, and the majority of those heterocycles are pyridines. In this paper, we survey <sup>1</sup>H-NMR properties of nonheme oxoiron(IV) complexes with pyridine ligands and find a correlation between the paramagnetically shifted pyridine protons observed with the torsion angles between the pyridine ring and the Fe=O unit. (See Scheme 1 for schematic structures of the oxoiron(IV) complexes studied.)



**Scheme 1** Schematic structures of the  $\text{Fe}^{\text{IV}}(\text{O})$  complexes in this study.

### **Experimental Section:**

All chemicals were purchased either from Sigma Aldrich, Alfa Aesar or TCI Chemicals. Deuterated solvents were used without purification. Elemental analyses were carried out by Atlantic Microlab (Norcross, GA). The syntheses of ligands, iron(II) and iron(IV) complexes are detailed below.

#### ***Syntheses of ligands:***

The precursors bis(2-pyridyl)methylamine<sup>20</sup> and 5-methyl-2-pyridylmethyl chloride hydrochloride<sup>21</sup> to the ligand 5Me<sub>2</sub>N4Py<sup>22</sup> and 5MeBnTPEN were synthesized according to a reported methods. The ligands Py5Me<sub>2</sub>,<sup>23-24</sup> N4Py<sup>25</sup>, BnTPEN<sup>26</sup>, 5MeBnTPEN<sup>15</sup> and TMC-py<sup>11, 27</sup> were synthesized according to reported procedures.

**5Me<sub>2</sub>N4Py** (*N,N*-bis((5-methyl-2-pyridinyl)methyl)-1,1-di(2-pyridinyl)methanamine)

5-Methyl-2-pyridylmethyl chloride hydrochloride (1.61 g, 9.1 mmol) was dissolved in water and neutralized with an equimolar amount of 5 M NaOH. The solution was added to a solution of bis(2-pyridyl)methylamine (0.84 g, 4.54 mmol) in CH<sub>2</sub>Cl<sub>2</sub> (1 mL) cooled to 0 °C. Additional 5 M NaOH (3 mL) was added and the solution was stirred at room temperature under argon for 48 hours. The solution was extracted with dichloromethane (3 x 20 mL) and the organics were combined, dried over Na<sub>2</sub>SO<sub>4</sub>, and concentrated to yield 5Me<sub>2</sub>N4Py as a red oil (1.7 g, 95% yield).

**Syntheses of iron(II) complexes:**

The iron(II) precursors supported by ligands Py5Me<sub>2</sub>,<sup>23</sup> N4Py,<sup>25</sup> BnTPEN,<sup>28</sup> and TMC-py<sup>11, 27</sup> were prepared according to reported procedures.

**[Fe(5Me<sub>2</sub>N4Py)(NCCH<sub>3</sub>)](ClO<sub>4</sub>)<sub>2</sub>** A solution of 5Me<sub>2</sub>N4Py (1.7 g, 4.3 mmol) in dichloromethane (5 mL) was added slowly to a solution of Fe(ClO<sub>4</sub>)<sub>2</sub>·xH<sub>2</sub>O (1.09 g, 4.3 mmol) in CH<sub>3</sub>CN (2 mL). The deep red solution was stirred for an additional 2 hours. Addition of ethyl acetate crashed out an orange-red powder. The powder was recrystallized from MeCN/ether to give orange-red crystals. Anal. Calcd. For Fe<sup>II</sup>(5Me<sub>2</sub>N4Py)(NCCH<sub>3</sub>)(ClO<sub>4</sub>)<sub>2</sub>, C<sub>27</sub>H<sub>28</sub>Cl<sub>2</sub>FeN<sub>6</sub>O<sub>8</sub>: C, 46.91; H, 4.08; N, 12.16. Found: C, 46.32; H, 4.08; N, 12.01.

**Syntheses of oxoiron(IV) complexes:**

Most iron(IV) complexes were synthesized as reported. The synthetic procedures for **1-5Me** and **5** are described below.

**[Fe<sup>IV</sup>(O)(5Me<sub>2</sub>N4Py)](ClO<sub>4</sub>)<sub>2</sub> (1-5Me)** NaClO<sub>4</sub> (140 mg, 1.14 mmol) and ceric ammonium nitrate (CAN) (125 mg, 0.23 mmol) were dissolved in 2 mL water to give a yellow solution. This mixture was then transferred to a solution of [Fe<sup>II</sup>(5Me<sub>2</sub>N4Py)(MeCN)](ClO<sub>4</sub>)<sub>2</sub> (45 mg, 0.065 mmol) in 1 mL acetonitrile to yield a blue solution. Slow evaporation of acetonitrile at 2-5 °C over the course of 2 days formed blue crystals suitable for X-ray diffraction, which were filtered, washed with 1 mL of water, and dried on a sintered frit for 2 hours (30 mg, 69%). Anal. calcd. for

$[\text{Fe}^{\text{IV}}(\text{O})(5\text{Me}_2\text{N}_4\text{Py})](\text{ClO}_4)_2 \cdot [0.5 \text{ H}_2\text{O} \cdot 0.5 \text{ MeCN}]$  or  $\text{C}_{26}\text{H}_{27.5}\text{Cl}_2\text{FeN}_{5.5}\text{O}_{9.5}$ : C, 44.88; H, 3.98; N, 11.07. Found: C, 45.04; H, 3.81; N, 11.04.

**$[\text{Fe}^{\text{IV}}(\text{O})(\text{Py}5\text{Me}_2)](\text{OTf})_2$  (5)** The complex was synthesized following the reported method.<sup>23</sup>

Our attempts to get a crystal structure of **5** as a triflate or perchlorate salt did not afford crystalline solids suitable for X-ray diffraction. In order to obtain diffraction quality crystals, a small amount of the iron(II) precursor (10 mg, 0.012 mmol) was dissolved in about 0.25 mL of MeCN, and 5 equiv. ceric ammonium nitrate (33 mg 0.06 mmol) in 0.75 mL of water was added as a solution. The solution was kept at 2-5 °C and afforded micro-crystalline solids suitable for X-ray diffraction after 8 h, with  $[\text{Ce}(\text{NO}_3)_6]^{2-}$  as the counterion.

#### ***<sup>1</sup>H-NMR Spectroscopy:***

<sup>1</sup>H-NMR spectra were recorded on a Bruker 400 MHz spectrometer at 298 K unless otherwise stated, with reported <sup>1</sup>H-NMR chemical shifts ( $\delta$  [ppm]) referenced to residual solvent peaks. 8" Wilmad-LabGlass 528-PP-7-5 NMR tubes were used to collect NMR spectra for iron(IV) complexes. If a lower temperature was used to collect any data, the NMR instrument's probe temperature was calibrated using a sealed NMR tube containing a solution of tetramethylsilane (TMS) and methanol as a standard. The following parameters were used to acquire the <sup>1</sup>H-NMR data for paramagnetic compounds: Acquisition time = 0.064 s; relaxation delay = 0.03 s; sweep width = 400 ppm offset (centered) at 6 ppm; line broadening factor = 10-30 Hz. The <sup>1</sup>H-NMR spectra obtained were processed either using the NMR processing software MestReNova 12.0 or through Bruker's Top-Spin 3.5pl7.

#### ***Crystallographic details:***

##### **$[\text{Fe}^{\text{IV}}(\text{O})(5\text{Me}_2\text{N}_4\text{Py})](\text{ClO}_4)_2$ (1-5Me)**

A crystal (approximate dimensions 0.200 x 0.200 x 0.050 mm) was placed onto the tip of a 0.5 mm MiTeGen loop and mounted on a Bruker Photon-II CMOS diffractometer for a data collection at 100(2) K.<sup>29</sup> A preliminary set of cell constants was calculated from

reflections harvested from three sets of 12 frames. These initial sets of frames were oriented such that orthogonal wedges of reciprocal space were surveyed. This produced initial orientation matrices determined from 298 reflections. The data collection was carried out using MoK $\alpha$  radiation (graphite monochromator) with a frame time of 40 seconds and a detector distance of 5.0 cm. A randomly oriented region of reciprocal space was surveyed to the extent of one sphere and to a resolution of 0.77 Å. Six major sections of frames were collected with 1° steps in  $\omega$  at four different  $\phi$  settings and a detector position of -28° in  $2\theta$ . The intensity data were corrected for absorption and decay.<sup>30</sup> Final cell constants were calculated from the xyz centroids of 3538 strong reflections from the actual data collection after integration.<sup>31</sup> Please refer to the table in SI for additional crystal and refinement information. The structure was solved using SHELXT 2014/5 (Sheldrick 2008)<sup>32</sup> and refined using SHELXL-2018/3 (Sheldrick, 2018).<sup>33</sup> The space group *I*bam was determined based on systematic absences and intensity statistics. A direct-methods solution was calculated which provided most non-hydrogen atoms from the E-map. Full-matrix least squares / difference Fourier cycles were performed which located the remaining non-hydrogen atoms. All non-hydrogen atoms were refined with anisotropic displacement parameters. All hydrogen atoms were placed in ideal positions and refined as riding atoms with relative isotropic displacement parameters. The final full matrix least squares refinement converged to  $R_1 = 0.0495$  and  $wR_2 = 0.1754$  (F<sup>2</sup>, all data). The asymmetric unit consists of the iron cation atoms Fe1, O1, and N1 lying on a crystallographic mirror plane. Additionally, within the asymmetric unit are three perchlorate anions lying on special positions. One perchlorate lies on a crystallographic 222 special position with a 0.25 occupancy. Another perchlorate anion is modeled over two positions (49:51) and lies along a crystallographic *n*-glide perpendicular to *c* and *b*-glide perpendicular to *a*. The oxygen atoms were refined in two parts of the same occupancy. Enhanced rigid-bond restraints were applied to the central chlorine Cl4 and its bound oxygen atoms O2, O3, O4, and O5. A third perchlorate anion was found on the same crystallographic mirror that bisects the iron cation, which caused severe disorder. The oxygen atoms are modeled over two positions (25:75) and enhanced rigid-bond restraints were applied to the perchlorate anion and thermal restraints were applied to two pairs of oxygen atoms to handle

correlation problems. Additionally, an acetonitrile was found in the asymmetric unit in 0.5 occupancy. The methyl group of the acetonitrile was found to be disordered due to the entire fragment being on the crystallographic mirror plane that bisects the iron cation. Thus, the full formula contains one iron cation, two perchlorate anions, and one acetonitrile solvent molecule.

### **[Fe<sup>IV</sup>(O)(Py5Me<sub>2</sub>)] [Ce(NO<sub>3</sub>)<sub>6</sub>]**

A crystal (approximate dimensions 0.100 x 0.050 x 0.030 mm) was placed onto the tip of a 0.5 mm MiTeGen loop and mounted on a Bruker Photon-II CMOS diffractometer for a data collection at 100(2) K.<sup>29</sup> A preliminary set of cell constants was calculated from reflections harvested from three sets of 12 frames. These initial sets of frames were oriented such that orthogonal wedges of reciprocal space were surveyed. This produced initial orientation matrices determined from 146 reflections. The data collection was carried out using MoK $\alpha$  radiation (graphite monochromator) with a frame time of 10 seconds and a detector distance of 6.0 cm. A randomly oriented region of reciprocal space was surveyed to the extent of one sphere and to a resolution of 0.84 Å. Four major sections of frames were collected with 0.30° steps in  $\omega$  at four different  $\phi$  settings and a detector position of -28° in  $2\theta$ . The intensity data were corrected for absorption and decay.<sup>30</sup> Final cell constants were calculated from the xyz centroids of 9975 strong reflections from the actual data collection after integration.<sup>31</sup> Please refer to the table in SI for additional crystal and refinement information. The structure was solved using SHELXS-97 (Sheldrick 2008)<sup>32</sup> and refined using SHELXL-2018/3 (Sheldrick, 2018).<sup>33</sup> The space group P-1 was determined based on systematic absences and intensity statistics. A direct-methods solution was calculated which provided most non-hydrogen atoms from the E-map. Full-matrix least squares / difference Fourier cycles were performed which located the remaining non-hydrogen atoms. All non-hydrogen atoms were refined with anisotropic displacement parameters. The [Ce(NO<sub>3</sub>)<sub>6</sub>]<sup>2-</sup> dianion was located at an inversion center, and one-half of its unique structure was disordered. This disorder was modeled using the SAME thermal displacement for the nitrate oxygen atoms that were disordered by a 90° rotation. All hydrogen atoms were placed in ideal positions and refined as riding atoms with relative

isotropic displacement parameters. The final full matrix least squares refinement converged to  $R1 = 0.0317$  and  $wR2 = 0.0606$  ( $F2$ , all data).

### ***Details for calculating $^1\text{H}$ -NMR shifts***

We optimized the structures of complexes **1**, **3** and **5** in Gaussian 16 (Rev. B01)<sup>34</sup> with modified B3LYP (labeled as B3LYP\* in the following) functionals (lop(3/76=1000001500) lop(3/77=0720008000) lop(3/78=0810010000)), a 6-31G(d',p') basis set and a built-in acetonitrile solvation model (scrf=(solvent=acetonitrile)). To obtain a more precise result, we ran the optimization with a small step size (opt=maxstep=10), while the default value of *maxstep* was 30. Then we performed  $^1\text{H}$ -NMR shift calculations by using the same functional but with a Dunning correlation-consistency basis set cc-pVTZ.

The calculations were carried out by following the protocols described by Bagno and coworkers.<sup>35-38</sup> Geometries were optimized starting from X-ray structures (when available) or from pre-optimized structures obtained by the MM2 force-field method (when the XRD structure is not available, for example for complex **3**). All the optimizations were performed at the B3LYP\*/6-31G(d',p') level. Final energies and NMR parameters were computed with the B3LYP\*/cc-pVTZ level.<sup>39</sup> All calculations were carried out with Gaussian 16.<sup>34</sup>

The calculated  $^1\text{H}$ -NMR shifts were determined by the following formula:<sup>19, 40</sup>

$$\sigma = \sigma_{ref} - (\sigma_{orb} + \sigma_{FC} + \sigma_{PC})$$

where  $\sigma_{ref} = 31.02$  ppm for TMS was obtained at the same theoretical level as those for the Fe(IV) complexes included in this study.  $\sigma_{orb}$  is the orbital contribution to the proton, which is equivalent to the shielding for diamagnetic systems. The Fermi contact term,  $\sigma_{FC}$ , which originates from the scalar interaction between magnetic field from unpaired electrons and the magnetic momentum of target proton, dominates the paramagnetic component in the  $^1\text{H}$ -NMR shift arising from the paramagnetic center. The Fermi contact term can be calculated from Fermi's hyperfine interaction parameters as the following:

$$\sigma_{FC} = \frac{2\pi}{\gamma_I} g_{iso} \mu_B A \frac{S(S+1)}{3kT}$$



in which  $\gamma_I$  is the magnetogyric ratio of the nucleus I and  $g_{iso}$  is the isotropic g factor of the spin system,  $\mu_B$  is the Bohr magneton and  $A$  is the Fermi hyperfine interaction parameter. The contribution from pseudo-contact term  $\sigma_{PC}$ , can be approximated by the theory developed by Hrobárik et al.<sup>41</sup> Usually it is small and can be ignored compared with  $\sigma_{FC}$ . In this work we estimate the  $^1\text{H}$ -NMR shift only by the orbital term and Fermi contact term. All calculations were done at 298 K, the same temperature at which most of the  $^1\text{H}$ -NMR measurements were performed in this work.

## Results and Discussion

### Complex 1

Complex **1** exhibits a well-resolved  $^1\text{H}$ -NMR spectrum with paramagnetically shifted resonances that span over a range of 200 ppm, as first reported by Klinker *et al.*<sup>15</sup> The sharper features in this spectrum correspond to protons farthest away from the  $S = 1$   $\text{Fe}^{\text{IV}}=\text{O}$  center and can be identified on the basis of their relative signal intensities and linewidths, methyl substitution experiments, and COSY cross peaks.<sup>15</sup> As expected, there are two sets of signals derived from comparably intense  $\beta$ ,  $\beta'$  and  $\gamma$  protons on the pyridine rings (Figure 1), with the  $\gamma$  protons being sharper due to their greater distance from the iron center. Interestingly, the signals of the  $\beta$  and  $\beta'$  pyridine protons of one pair (subset **a**) are observed at 44 and  $-17$  ppm, corresponding to paramagnetic shifts ( $\Delta_{\text{paramagnetic}}$ ) of  $+37$  and  $-24$  ppm relative to about 7 ppm chemical shift for the pyridine  $\beta$  protons of the unmetalated N4Py ligand. The assignments for the  $\beta$  proton signals in this set can be further confirmed by the  $^1\text{H}$ -NMR spectrum of the corresponding  $[\text{Fe}^{\text{IV}}(\text{O})(5\text{Me}_2\text{N4Py})]^{2+}$  (**1-5Me**;  $5\text{Me}_2\text{N4Py} = N,N\text{-bis}((5\text{-methylpyridin-2-yl)methyl})\text{-1,1-di(pyridin-2-yl)methan-amine}$ ) complex in Figure 1, where the signal for these protons disappears when the  $\beta\text{-H}$  protons of this set of pyridines are replaced with methyl groups. On the other hand, the signals for the  $\beta$  and  $\beta'$  pyridine protons of the other pair (subset **b**) are observed at 30 and  $-11$  ppm, corresponding to  $\Delta_{\text{paramagnetic}}$  values of  $+23$  and  $-18$  ppm. Thus, the  $\beta$  and  $\beta'$  protons of subset **a** exhibit paramagnetic shifts respectively 60% and 30% larger than found for the  $\beta$  and  $\beta'$  protons in subset **b**.

Clearly the pyridine  $\beta$  protons of the former pair sense a larger amount of unpaired spin density than those in the latter pair.

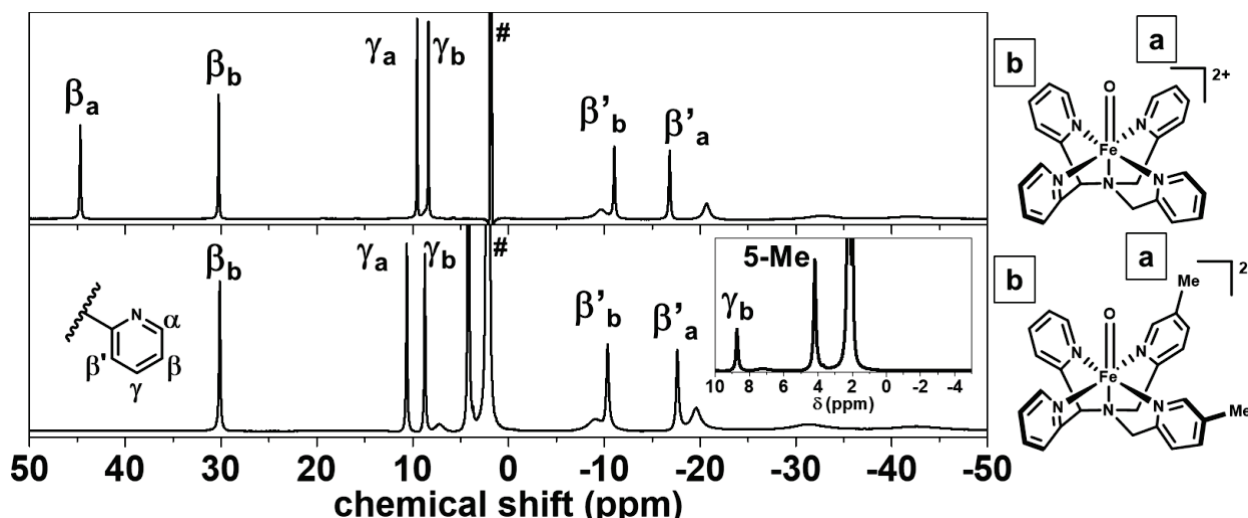


**Figure 1** Top panel:  $^1\text{H}$ -NMR spectra of **1** (top) and **1-5Me** (bottom) in  $\text{CD}_3\text{CN}$  at 298 K. Inset from -5 to 10 ppm shows the 5-Me proton signals. # = residual solvent.

### Other Complexes Based on Modifications of the N4Py Ligand

The  $^1\text{H}$ -NMR spectra of  $[\text{Fe}^{\text{IV}}(\text{O})(\text{N2Py2B})]^{2+}$  (**2-B**) ( $\text{N2Py2B}$  = *N,N*-bis((1-methyl-1*H*-benzo[*d*]imidazol-2-yl)methyl)-1,1-di(pyridin-2-yl)methanamine) and  $[\text{Fe}^{\text{IV}}(\text{O})(\text{N2Py2Q})]^{2+}$  (**2-Q**) ( $\text{N2Py2Q}$  = 1,1-di(pyridin-2-yl)-*N,N*-bis(quinolin-2-ylmethyl)methanamine) in acetonitrile at 298 K have also been recently reported. The pyridine proton shifts in these complexes fall under subset **b**. In complex **2-B**, the  $\beta$  and  $\beta'$  proton signals are respectively found at 34 and -9.6 ppm, and they are distinct from the signals of benzimidazole protons, which lie between 0-15 ppm and have been discussed.<sup>42</sup> Similarly, the  $\beta$  and  $\beta'$  proton signals are found respectively at 26 and -11.7 ppm in **2-Q**.<sup>43</sup>

On the other hand,  $[\text{Fe}^{\text{IV}}(\text{O})((6'\text{-ArF})_2\text{N4Py})]^{2+}$  (**1-6'ArF<sub>2</sub>**;  $(6'\text{-ArF})_2\text{N4Py}$  = 1,1-bis(6-(2,6-difluorophenyl)pyridin-2-yl)-*N,N*-bis(pyridin-2-ylmethyl)methanamine) is an N4Py derivative in which the other pyridine pair has been modified by the introduction of a 2,6-difluorophenyl substituent at the alpha positions of the two pyridines that are linked to the tertiary amine via a common methine carbon.<sup>16</sup> In this case, the  $^1\text{H}$ -NMR spectrum of the complex was reported at 253 K by the authors in the Supporting Information of

their paper but not assigned. In comparing this  $^1\text{H}$ -NMR spectrum with those we obtained for **1** and **1-5Me**, we could confidently identify the  $\beta$  pyridine protons of the unsubstituted pyridine donors to the peak at 48 ppm based on similarities in chemical shift and linewidth, thereby assigning them as belonging to subset **a**. There are other variants of complex **1** (like **1-5Me**) for which  $^1\text{H}$ -NMR spectra have been reported at 298 K. In one case the methine proton of the ligand framework is substituted with a methyl group,<sup>44</sup> while in the other case pyridine ring protons are substituted by methyl and methoxy groups.<sup>45</sup> However these complexes have similar chemical shifts for  $\beta$  protons as **1** and **1-5Me**, so they are not extensively discussed in this work.

Also reported at 298 K are the  $^1\text{H}$ -NMR spectra of the two  $[\text{Fe}^{\text{IV}}(\text{O})(\text{N4Py})]^{2+}$  variants in which 6-methyl substituents have been introduced on the pyridines in subsets **a** or **b**.<sup>46-47</sup> These complexes are referred to as **1-6Me** and **1-6'Me** in this work. The signals for the  $\beta$  protons in the unsubstituted pair of pyridines of these complexes have been assigned based on comparisons of chemical shift and linewidth with those of the parent complex **1** (Table 1). For **1-6Me** the pyridine  $\beta$ -H signal for the unsubstituted pyridines belonging to subset **b** is found at 25 ppm, while the  $\beta$ -H signal for the unsubstituted pyridine belonging to subset **a** is found at 46 ppm for **1-6'Me**, matching values found for corresponding protons in **1**. Further comparisons with the  $^1\text{H}$ -NMR spectra of **1** and **1-5Me** allow us to tentatively assign the  $\gamma_a$  and  $\beta'_a/\beta'_b$  proton signals in **1-6Me** and **1-6'Me** (Table 1) from their reported spectra.<sup>46</sup> The  $\beta'_a$  and  $\beta'_b$  signals in **1-6Me** likely overlap with each other at -12.4 ppm, based on the doubled intensity of this peak, but the  $\beta'_a$  and  $\beta'_b$  signals in **1-6'Me** are distinguishable at -17.2 and -8.6 ppm. The  $\gamma_a$  proton signals are likely the sharp downfield shifted peaks at 10.6 and 10.3 ppm in the spectra of **1-6Me** and **1-6'Me**.

### Complexes 3 and 4

The  $^1\text{H}$ -NMR spectrum of the related  $[\text{Fe}^{\text{IV}}(\text{O})(\text{BnTPEN})]^{2+}$  (**3**; BnTPEN = *N'*-benzyl-*N,N,N*-tris(pyridin-2-ylmethyl)ethane-1,2-diamine) complex (Figure 2) has been reported previously and shows three different sets of pyridine proton signals in a 1:1:1 ratio that were assigned using methyl substitutions and COSY methods.<sup>15</sup> Two of the pyridines exhibit  $\beta$  protons with  $^1\text{H}$ -NMR shifts of 43 and 40 ppm, comparable to the more

downfield shifted pair in **1**, but there is a difference in shifts because ring **a** is trans to a pyridine, while ring **a'** is trans to a tertiary amine. Intriguingly the  $\beta$  proton signal of the third pyridine (ring **c**) is found in the upfield region with a chemical shift of  $-0.3$  ppm, representing an 8-ppm  $\Delta_{\text{paramagnetic}}$  shift relative to the free ligand. This paramagnetic shift is much smaller than found for the  $\beta$  protons in rings **a** and **a'** and opposite in sign. This  $\beta$  proton signal assignment is further confirmed by the  $^1\text{H}$ -NMR spectrum of  $[\text{Fe}^{\text{IV}}(\text{O})(5\text{MeBnTPEN})]^{2+}$  (**3-5Me**; 5MeBnTPEN = *N'*-benzyl-*N'*-((5-methylpyridin-2-yl)methyl)-*N,N*-tris(pyridin-2-ylmethyl)ethane-1,2-diamine) where the  $\beta$  proton signal of this pyridine disappears when the 5-H atom of this pyridine is replaced with a methyl group (Figure 2).<sup>15</sup> The observed perpendicular orientation of ring **c** relative to the Fe=O axis, as suggested by the crystal structure of its iron(II) precursor  $[\text{Fe}^{\text{II}}(\text{BnTPEN})(\text{NCMe})]^{2+}$ ,<sup>48</sup> provides an easy rationale for the chemical shift differences observed, but the principle that controls the magnitude and sign of the paramagnetic shift ( $\Delta_{\text{paramagnetic}}$ ) remains to be established.

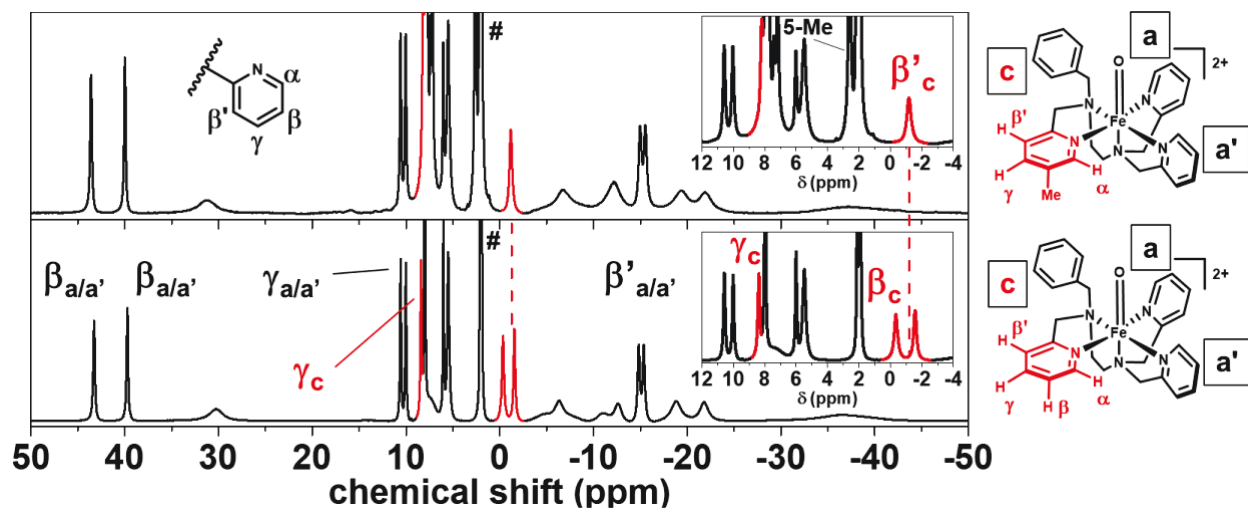


**Figure 2** The  $^1\text{H}$ -NMR spectra of **3** and **3-5Me** in  $\text{CD}_3\text{CN}$  at 298 K. Insets show expanded regions from  $-4$  to  $12$  ppm. Signals in red indicate those arising from the subset **c** pyridine. # = residual solvent.

The shift patterns observed for **3** are corroborated by the  $^1\text{H}$ -NMR spectrum of  $[\text{Fe}^{\text{IV}}(\text{O})(\text{Py}_2\text{MeTACN})]^{2+}$  (**4**;  $\text{Py}_2\text{MeTACN}$  = 1-methyl-4,7-bis(pyridin-2-ylmethyl)-1,4,7-triazonane), which was reported by Costas and co-workers.<sup>49</sup> This complex has two pyridine donors, one parallel to the Fe=O unit and the other perpendicular to it. The

shifts observed for the  $\beta$ ,  $\beta'$  and  $\gamma$  protons on the pyridine parallel to the Fe=O unit are similar to those found for subset **a** in **1** and **3**, while the shifts for the protons on the perpendicular pyridine correspond to values found for the corresponding perpendicular pyridine in **3** (Table 1).

### Complexes 5 and 6

The  $^1\text{H}$ -NMR spectrum of yet another  $[\text{Fe}^{\text{IV}}(\text{O})(\text{N}5)]^{2+}$  complex provides additional information that sheds light on what structural features may dictate the differences in chemical shifts observed. This complex, namely  $[\text{Fe}^{\text{IV}}(\text{O})(\text{Py}5\text{Me}_2)]^{2+}$  (**5**;  $\text{Py}5\text{Me}_2$  = 2,6-bis(1,1-bis(2-pyridyl)ethyl)-pyridine), was first described by Chang and co-workers<sup>23</sup> and has a pentadentate N5 ligand with four pyridine rings connected to a common pyridine ring that is bound trans to the Fe=O unit (see below for a discussion of its crystal structure). The four pyridines are bound in the equatorial plane relative to the Fe=O unit and are equivalent to each other by virtue of the effective  $C_{2v}$  symmetry of the complex. As a result, only one set of pyridyl  $\beta$  and  $\beta'$  proton signals is observed at 27 and -12 ppm, chemical shift values that are close to but smaller than those found for the pyridine  $\beta$  and  $\beta'$  protons in subset **b** of **1** (Figure 3). While the assignments of these signals to pyridine  $\beta$  and  $\beta'$  protons are not in doubt, a rationale for the range of shifts observed for complexes **1** – **6** is desirable.

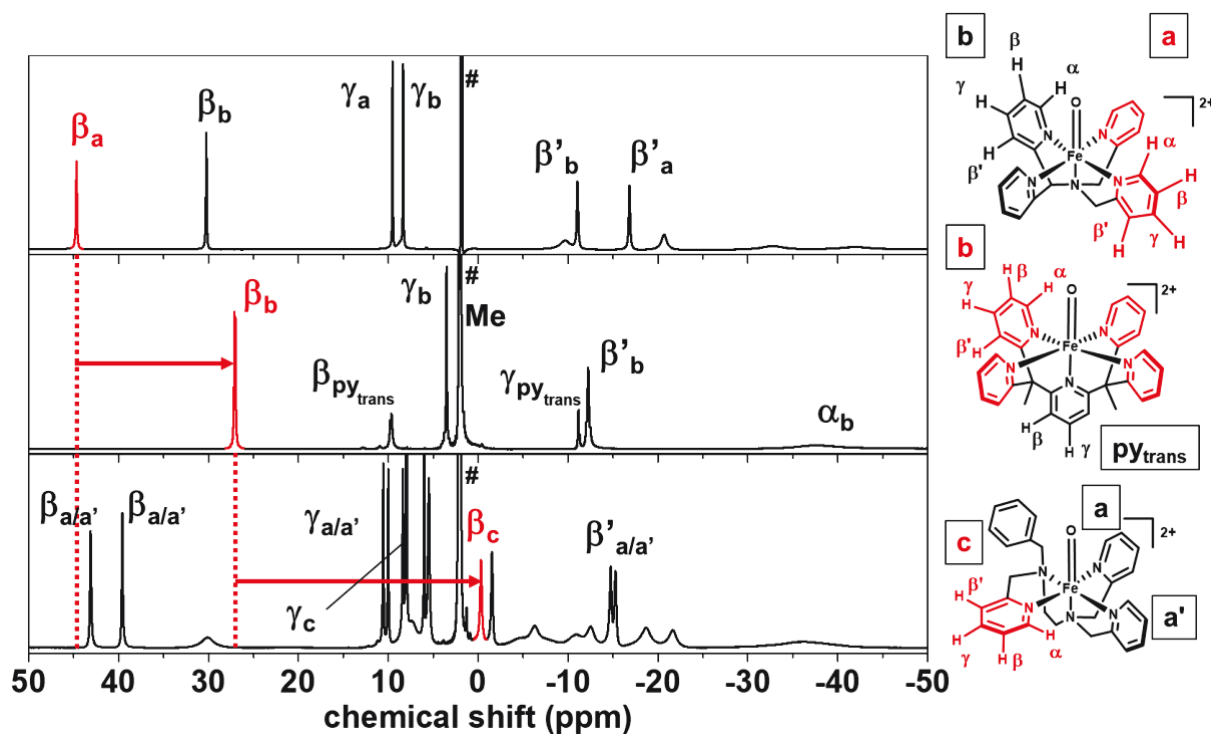


**Figure 3**  $^1\text{H}$ -NMR spectra of **1** (top), **5** (middle) and **3** (bottom) in  $\text{CD}_3\text{CN}$  at 298 K. The equatorial  $\beta$  proton signals in orientation **a**, **b** and **c** are highlighted in red. # = residual solvent, overlapped with methyl group in the  $^1\text{H}$ -NMR spectrum of **5**.

In addition, there is a fifth pyridine in **5** that is bound trans to the oxo ligand. Its distinct coordination mode gives rise to quite a different shift pattern, with the  $\beta$  proton signals only slightly downfield shifted to 10 ppm that corresponds to a  $\Delta_{\text{paramagnetic}}$  value of only 3 ppm. On the other hand, the  $\gamma$  proton signal shifts upfield to -11 ppm, or a  $\Delta_{\text{paramagnetic}}$  value of about -18 ppm, which is quite large relative to the  $\gamma$  proton signals of the other complexes (Table 1). A similar shift pattern is found for the protons of the pyridine bound trans to the oxo moiety in  $[\text{Fe}^{\text{IV}}(\text{O})(\text{TMC-py})]^{2+}$  (**6**; TMC-py = 1-(pyridyl-2-methyl)-4,8,11-trimethyl-1,4,8,11-tetrazacyclotetradecane),<sup>27</sup> for which the  $\beta$  proton signals are found at 7 and 11 ppm, an average of 9 ppm (or a  $\Delta_{\text{paramagnetic}}$  of only 2 ppm) and the  $\gamma$  proton signal shifted upfield to -5 ppm ( $\Delta_{\text{paramagnetic}} = -12$  ppm) (Figure 4). However, the  $^1\text{H}$ -NMR spectrum of **6** has additional peaks that need assignment.

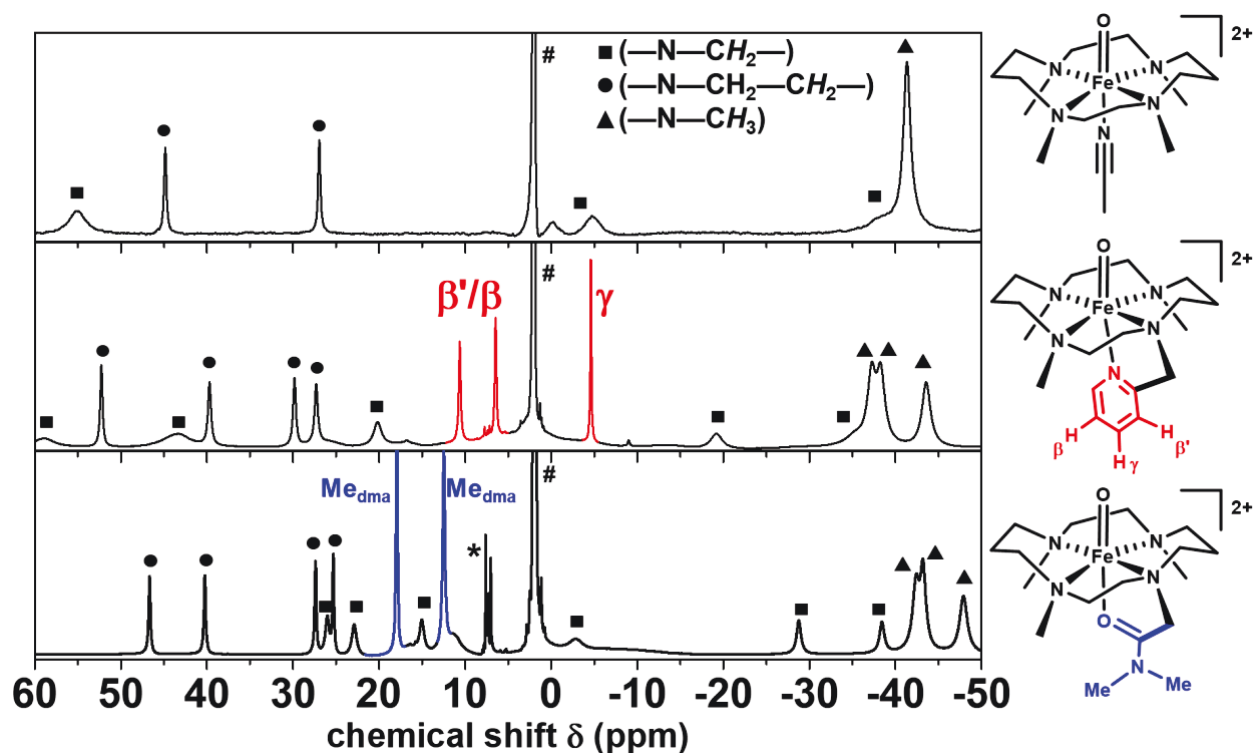


**Figure 4**  $^1\text{H-NMR}$  spectra of  $[\text{Fe}^{\text{IV}}(\text{O})(\text{TMC})(\text{NCMe})]^{2+}$  (top),  $[\text{Fe}^{\text{IV}}(\text{O})(\text{TMC-py})]^{2+}$  (**6**) (middle) and  $[\text{Fe}^{\text{IV}}(\text{O})(\text{TMC-dma})]^{2+}$  (bottom) in  $\text{CD}_3\text{CN}$  at 298 K. Peaks associated with the oxidant are designated by \*. See SI for full spectra. # = residual solvent.

The non-pyridine-based peaks of **6** can be assigned by comparison with the  $^1\text{H-NMR}$  spectra of the more symmetric parent complex  $[\text{Fe}^{\text{IV}}(\text{O})(\text{TMC})(\text{NCMe})]^{2+}$  and the less symmetric but fully assigned complex  $[\text{Fe}^{\text{IV}}(\text{O})(\text{TMC-dma})]^{2+}$  (where TMC-dma = *N,N*-dimethyl-2-(4,8,11-trimethyl-1,4,8,11-tetraazacyclotetradecan-1-yl)acetamide).<sup>12</sup>

$[\text{Fe}^{\text{IV}}(\text{O})(\text{TMC})(\text{NCMe})]^{2+}$  contains only methylene and methyl protons and, due to its  $\text{C}_{2v}$  symmetry, exhibits relatively distinct resonances that are easily distinguished from each other based on their relative intensities.<sup>13</sup> In addition, the  $^1\text{H-NMR}$  spectral pattern associated with  $[\text{Fe}^{\text{IV}}(\text{O})(\text{TMC-dma})]^{2+}$  somewhat resembles that of **6**.

**Table 1**  $^1\text{H}$ -NMR chemical shifts observed for pyridine  $\beta$  and  $\gamma$  protons of oxoiron(IV) complexes. Available DFT-calculated values are listed in parentheses, and unpaired spin density values in atomic units  $\times 10^{-4}$  are shown in square brackets.

$\text{Fe}^{\text{IV}}(\text{O}), \text{L} =$	T (K)	$\beta_a, \beta_b$ or $\beta_c$	$\beta'_a, \beta'_b$ or $\beta'_c$	$\gamma_a, \gamma_b$ or $\gamma_c$
N4Py ( <b>1</b> ) <sup>15</sup>	298	$\beta_a$ 44 (48) [2.5], $\beta_b$ 30 (33) [1.5]	$\beta'_a$ -17 (-18) [-1.6], $\beta'_b$ -11 (-12) [-1.2]	$\gamma_a$ 9.5 (9.0) [0.0], $\gamma_b$ 8.3 (8.9) [0.0]
(5-Me) <sub>2</sub> N4Py ( <b>1-5Me</b> )	298	5Me: 4.2, $\beta_b$ 30	$\beta'_a$ -17.6, $\beta'_b$ -10.3	$\gamma_a$ 10.6, $\gamma_b$ 8.7
(6-Me) <sub>2</sub> N4Py <sup>‡</sup> ( <b>1-6Me</b> ) <sup>46</sup>	298	$\beta_b$ 25	$\beta'_a$ -12.4, $\beta'_b$ -12.4	$\gamma_a$ 10.6
(6'-Me) <sub>2</sub> N4Py <sup>‡</sup> ( <b>1-6'Me</b> ) <sup>46</sup>	298	$\beta_a$ 44	$\beta'_a$ -17.2, $\beta'_b$ -8.6	$\gamma_a$ 10.3
(6'-ArF <sub>2</sub> ) <sub>2</sub> -N4Py <sup>#</sup> ( <b>1-6'ArF<sub>2</sub></b> ) <sup>16</sup>	253	$\beta_a$ 48		
N2Py2B ( <b>2-B</b> ) <sup>42</sup>	298	$\beta_b$ 34	$\beta'_b$ -9.6	$\gamma_b$ 8.6
N2Py2Q ( <b>2-Q</b> ) <sup>43</sup>	298	$\beta_b$ 26	$\beta'_b$ -11.7	
BnTPEN ( <b>3</b> ) <sup>15</sup>	298	$\beta_a$ 43 (47) [2.4], $\beta_{a'}$ 40 (42) [2.1], $\beta_c$ -0.3 (-3.7) [-0.7]	$\beta'_a$ -15.3 (-18) [-1.6], $\beta'_{a'}$ -14.7 (-15) [-1.5], $\beta'_c$ -1.5 (-2.7) [-0.6]	$\gamma_a$ 10.6 (9.2) [0.0], $\gamma_{a'}$ 10.0 (9.2) [0.0], $\gamma_c$ 8.4 (13.7) [0.3]
5-Me-BnTPEN ( <b>3-5Me</b> ) <sup>15</sup>	298	$\beta_a$ 43.6, $\beta_{a'}$ 40, 5Me: 2.6	$\beta'_a$ -15, $\beta'_{a'}$ -15.5, $\beta'_c$ -1.2	$\gamma_a$ 10.6, $\gamma_{a'}$ 10, $\gamma_c$ 8.2
Py <sub>2</sub> MeTACN ( <b>4</b> ) <sup>49</sup>	300	$\beta_a$ 46, $\beta_c$ -1.4	$\beta'_a$ -13, $\beta'_c \approx 1.5$	$\gamma_a$ 13.3, $\gamma_c$ 11.2
Py <sub>5</sub> Me <sub>2</sub> ( <b>5</b> )	298	$\beta_b$ 27 (27.9) [1.3], $\beta_{\text{trans}}$ 9.7 (7.8) [0.0]	$\beta'_b$ -12 (-15) [-1.4], $\beta'_{\text{trans}}$ 9.7 (7.8) [0.0]	$\gamma_b$ 3.5 (3.0) [-0.3], $\gamma_{\text{trans}}$ -11.1 (-7.2) [1.0]
TMC-py ( <b>6</b> ) <sup>27</sup>	298	$\beta_{\text{trans}}$ or $\beta'_{\text{trans}}$ 10.6 or 6.5		$\gamma_{\text{trans}}$ -4.6

All  $\alpha$ -H proton signals assigned are based on DFT, except for complex **5**, which is found at -38 ppm.

<sup>‡</sup> We reassigned some resonances reported for **1-6Me** and **1-6'Me** in ref. 46 based on a comparison with the resonances and linewidths observed in **1** and **1-5Me**.

<sup>#</sup> The  $^1\text{H}$ -NMR spectrum of **1-6'ArF<sub>2</sub>** was reported in ref. 16, but the signals were not specifically assigned. We have assigned the  $\beta_a$  proton to the 48-ppm peak, because it has a chemical shift and linewidth similar to the corresponding protons of **1**.



## DFT Calculations of Experimentally Observed $^1\text{H}$ -NMR Chemical Shifts

To further aid in the assignments of the  $^1\text{H}$ -NMR features of the oxoiron(IV) complexes in this study, we have applied the DFT approach adopted by Borgogno *et al.*<sup>35</sup> to calculate (see SI for details) the paramagnetic shifts of the protons in **1**, **3** and **5**. As illustrated in Figure 5 and Tables 1 and S3-S5, the calculated  $^1\text{H}$ -NMR shifts nicely reproduce our experimental observations. For example, in the case of **1**, the large downfield shifts of the  $\beta$  protons from two different pyridines are reproduced well, as are the smaller upfield shifts of the corresponding  $\beta'$  protons. Also predicted well are the respective downfield and upfield shifts for the  $\beta$  and  $\beta'$  protons on the four pyridines parallel to the Fe=O unit in **5**, which are similar to those in subset **b** pyridines in **1**. On the other hand, the  $^1\text{H}$ -NMR properties of the protons on the pyridine bound trans to the oxo atom in **5** are quite different. In this case, the  $\beta$  protons are hardly shifted, compared to the value of the free ligand, while the  $\gamma$  proton is found at  $-11$  ppm, corresponding to a  $\Delta_{\text{paramagnetic}}$  value of  $-18$  ppm, a shift pattern also predicted by DFT. The  $^1\text{H}$ -NMR properties of **3** serve as a third example. In this case, the protons on the two pyridines parallel to the Fe=O unit behave like subset **a** pyridines in **1** and predicted to behave accordingly by DFT. The third pyridine is oriented such that its plane is approximately perpendicular to the Fe=O unit. For this geometry, the  $\beta$  protons are shifted upfield while the  $\gamma$  proton is shifted downfield, a pattern predicted by DFT as well.

We note that our calculations do not consider the pseudo-contact contribution to the hyperfine shift. Given the relatively good agreement between experimental data and DFT predictions, the pseudo-contact contributions are likely to be small when compared with the contact contributions. The small discrepancies between calculated and experimental shifts presented in Table 1 or Figure 5 may originate from this approximation. Overall, however, there is good agreement between experiment and theory.

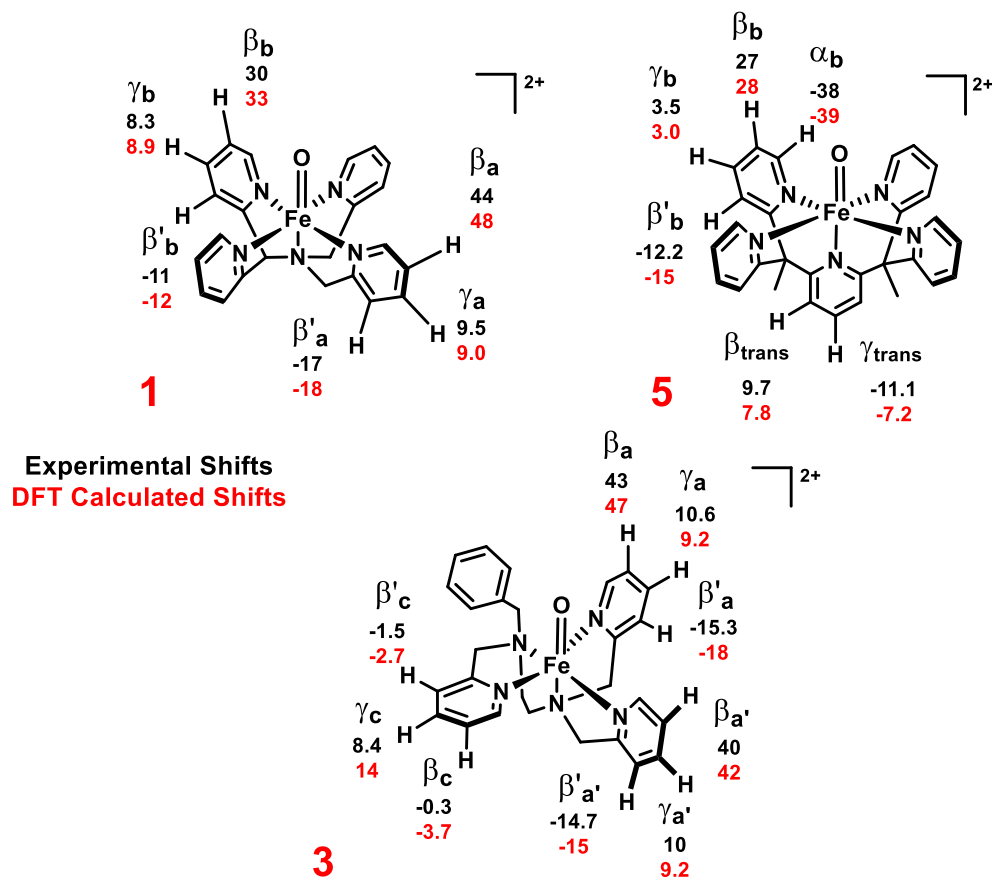


**Figure 5** Chemical shifts (in ppm) observed experimentally for **1**, **3** and **5** (black) and predicted by DFT (red).

### Correlation of the $^1\text{H}$ -NMR shifts with structure

We have obtained crystal structures of **1-5Me** and **5** (Figure 6) to complement the structural data already available for **1** and **6**<sup>11, 15</sup> and discern their relationships with chemical shifts. Unsurprisingly, **1-5Me** and **1** share similarities in their bond metrics and angles. Complex **1-5Me** shows an Fe=O bond length of 1.654(2) Å, which is essentially characteristic of oxoiron(IV) complexes. The amine trans to the oxo ligand has an Fe–N bond length of 2.042(3) Å and, as in **1**, it is the longest metal–ligand bond in the molecule. The iron center in the nearly collinear O=Fe–N<sub>amine</sub> unit subtends an angle of 178.2(1)°, similar to that found in **1** (Table 2). The equatorial pyridines **a** and **b** in **1-5Me** have Fe–N bond lengths of 1.946(2) Å and 1.964(2) Å, respectively, that are identical to the ones found in **1**, but with a smaller uncertainty. Overall, the pyridine subset **b** in **1**

and **1-5Me** gives rise to respective torsion angles of  $21.1(7)^\circ$  and  $30.4(2)^\circ$  with the oxoiron(IV) unit. These values are larger than those for the pyridines in set **a**, which have respective angles of  $13.9(5)^\circ$  and  $6.8(2)^\circ$  with the oxoiron(IV) unit (Scheme 2).

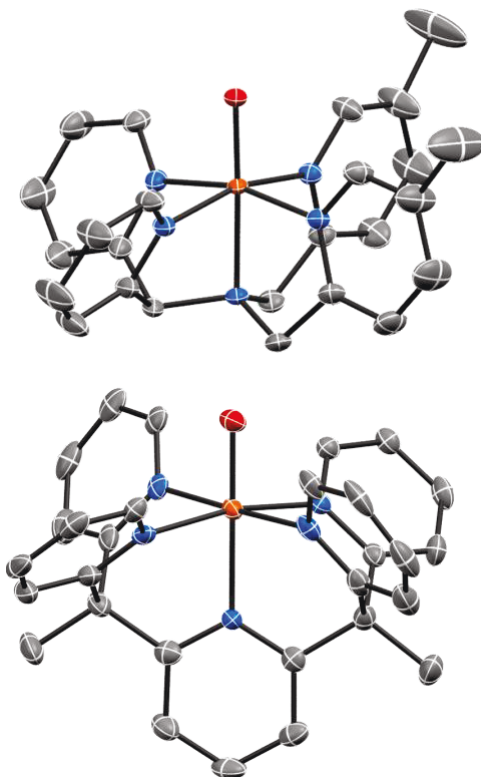


**Figure 6** Crystal structures of **1-5Me** (top) and **5** (bottom), shown using ORTEP plots with thermal ellipsoids set at 50% probability for **1-5Me** and 70% probability for **5**. Counterions, solvent and hydrogen atoms removed for clarity. See Supporting Information for more crystallographic details.

Complex **5** also shows a nearly linear  $\text{O}=\text{Fe}-\text{N}_{\text{pyridine}}$  axis with its iron center having an almost straight angle of  $179.8(1)^\circ$ . The approximately  $C_{2v}$ -symmetric solid-state structure has equatorial pyridines that can be all classified into the subset **b**. These pyridines have torsion angles of  $28.6(2)^\circ$ ,  $29.5(2)^\circ$ ,  $43.9(2)^\circ$  and  $44.2(2)^\circ$  relative to the oxoiron(IV) unit, and have Fe–N bond lengths ranging between 2.003(2) to 2.007(2) Å. Its Fe=O bond length is 1.656(2) Å. The pyridine trans to the oxoiron(IV) unit in **5** has a longer bond at 2.070(3) Å than its equatorial counterparts, but it is comparable to that in **6** (2.118(3) Å), which can be attributed to the trans effect of the oxo ligand.

**Table 2** Bond metrics for complexes examined in this work.

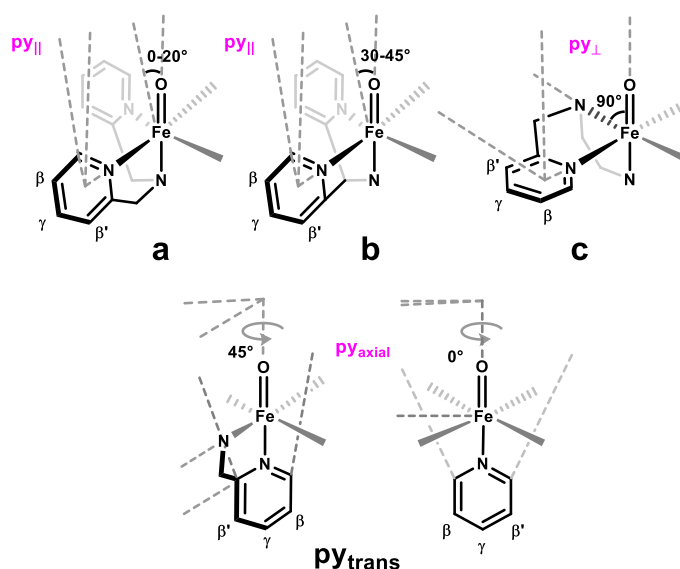
bond metrics	1	1-5Me	1-6Me	1-6'Me	1-6'ArF <sub>2</sub>	2-B	2-Q	3	4	5	6
r(Fe=O), Å	1.639(5)	1.654(2)			1.6600(16)	1.656(4)	1.677(4)			1.656(2)	1.667(4)
r(Fe–N <sub>eq</sub> ), Å	1.949(5)	1.946(2)			1.9730(18)	1.950(5)	2.073(4)			2.003(2)	2.103(6)
r(Fe–N <sub>eq</sub> ), Å					1.9771(18)	1.954(5)	2.067(2)			2.003(2)	2.100(5)
r(Fe–N' <sub>eq</sub> ),* Å	1.964(5)	1.964(2)			2.0269(17)	1.995(5)	2.023(4)			2.006(2)	2.054(4)
r(Fe–N' <sub>eq</sub> ),* Å					2.0408(17)	1.983(5)	2.022(4)			2.007(2)	2.075(6)
r(Fe–N <sub>ax</sub> ), Å	2.033(8)	2.042(3)			2.0511(17)	2.115(6)	2.084(4)			2.070(3)	2.118(3)
r <sub>av</sub> (Fe–N), Å	1.972	1.973			2.014	1.999	2.053			2.018	2.090
∠(O=Fe–N <sub>ax</sub> ), °	179.4(3)	178.2(1)			177.40(8)	177.0(2)	170.5(2)			179.8(1)	169.8(2)
Torsion angles, <sup>#</sup> ∠(O=Fe–N <sub>py</sub> –C <sub>α</sub> ), °	13.9(5)	6.8(2)	14.3(4), 19.7(4)	11.8(1), 16.4(1)	6.1(2), 13.6(2)			∥ 6.1(4) ∥' 16.1(4) ⊥ 91.4(4)	∥' 12.0(2), 14.7(2) ⊥ 100.8(2), 102.7(2)	43.9(2), 28.6(2), 44.2(2), 29.5(2)	
∠(O=Fe–N' <sub>py</sub> –C <sub>α</sub> ), °	21.1(7)	30.4(2)	33.2(4), 33.8(4)	29.0(1), 28.1(1)	23.5(2), 27.3(2)	25.4(2), 26.2(2)	29.3(4), 30.2(4)				
reference	<sup>15</sup>	this work	<sup>50</sup>	<sup>46-47</sup>	<sup>16</sup>	<sup>17</sup>	<sup>17</sup>	<sup>48</sup>		this work	<sup>11</sup>

\*For the N4Py-based complexes, the prime designation refers to the modified pyridines connected via the methine carbon atom.

<sup>#</sup>Crystal structures for **1-6Me**, **1-6'Me**, **3**, and **4** have not been reported, so no bond metrics are listed for these complexes, except for the torsion angles, which are obtained from the corresponding iron(II) structures. The crystal structure of the iron(II) precursor for complex **4** has two molecules in the asymmetric unit cell, so both the angles are listed.

When the accumulated  $^1\text{H}$ -NMR data on nonheme oxoiron(IV) complexes presented here are assessed as a whole, a pattern emerges. Complexes **1**, **1-5Me**, **1-6'Me**, **1-6'ArF<sub>2</sub>**, **3** and **4** have 2-picolyl groups that are mostly classified as subset **a** with  $\beta$ -pyridyl protons that are downfield shifted to 40-50 ppm. On the other hand, the pyridines represented by subset **b** are linked to the rest of the polydentate ligand framework via a methine carbon atom, as found in **1**, **1-5Me**, **2-Q**, **2-B** and **5**, and exhibit smaller downfield shifts for the  $\beta$ -pyridyl protons of  $\approx$  30 ppm. Yet a third subset designated as **c** consists of  $\beta$ -pyridyl protons with small upfield shifts. A look at the crystallographic data of oxoiron(IV) complexes suggests that these distinct sets of equatorially bound pyridines are oriented differently relative to the oxoiron(IV) unit, and the torsion angles for the four pyridines in subset **b** relative to the Fe=O unit ( $20^\circ$ - $45^\circ$ ) are larger than those of the pyridines in subset **a** ( $0^\circ$ - $14^\circ$ ). In the case of **5**, its crystal structure shows four different torsion angles for the equatorially bound pyridines that would classify them under subset **b**, but its  $^1\text{H}$ -NMR spectrum in  $\text{CD}_3\text{CN}$  shows only one signal for this set of pyridines, indicating that they are effectively equivalent in solution, presumably because they have sufficient flexibility in solution to average out its torsion angles. Complexes **3** and **4** each have a pyridine ligand that belongs to subset **c**, which corresponds to a pyridine arm that is likely approximately perpendicular to the oxoiron(IV) unit. This pyridine also exhibits the smallest paramagnetic shifts for its protons relative to the other pyridines.

This collected information is useful because a significant number of synthetic tetragonal oxoiron(IV) complexes reported thus far contain a pyridine heterocycle, and our analysis of these complexes highlights the three ways for this heterocycle to be oriented when bound *cis* to the  $\text{Fe}^{\text{IV}}=\text{O}$  unit (Scheme 2). In addition, there are oxoiron(IV) complexes with a pyridine bound *trans* to the Fe=O unit, either eclipsed with or staggered between the equatorial ligands, and these are also included in Scheme 2.



**Scheme 2** Comparison of the different orientations of pyridines relative to the oxoiron(IV) center in the complexes discussed in the study.

When the structural and solution-state data for these complexes are examined together, a remarkable dependence of the chemical shifts with pyridine torsion angles emerges. The paramagnetic shifts of the pyridine  $\beta$  and  $\beta'$  protons become smaller as the torsion angles increase. When the chemical shifts of the  $\beta$  protons in our collection of oxoiron(IV) complexes are plotted against the torsion angles, a reasonably linear correlation can be obtained. The torsion angle of pyridine **c** in complex **3** with the oxoiron(IV) unit can be deduced from the crystal structure of the low-spin iron(II) complex  $[\text{Fe}^{\text{II}}(\text{BnTPEN})(\text{NCMe})]^{2+}$ ,<sup>48</sup> which shows this pyridine to be almost orthogonal to the Fe–NCMe axis at  $91.4(4)^\circ$ . Its  $\beta$  proton is observed at  $-0.3$  ppm, while pyridines **a** and **a'** in complex **3** are likely parallel to the oxoiron(IV) unit. In the crystal structure of the iron(II) complex bound by acetonitrile, the pyridine **a'** has more torsional rotation than **a**, a consequence likely arising from steric interactions of pyridine **a'** protons with pyridine **c**.<sup>48</sup> This means that the more downfield shifted peak in **3** likely belongs to pyridine **a**, because its iron(II) complex shows a smaller torsion angle relative to the Fe–NCMe axis.

The torsion angle of pyridine **c** in complex **4** with the Fe=O unit can be deduced from the crystal structure of its iron(II) precursor,  $[\text{Fe}^{\text{II}}(\text{Py}_2\text{MeTACN})(\text{NCMe})]^{2+}$ , where one of the pyridines has a torsion angle with the Fe–NCMe that ranges from 100–103° (two molecules were found in the asymmetric unit cell, see Table 2), and its  $\beta$ -H signal in the corresponding complex **4** is observed at  $\approx 1.5$  ppm. Similarly, complex **4** also likely has a picolyl group aligned roughly parallel to the Fe=O unit (pyridine subset **a**), with its  $\beta$ -H shift at 46.5 ppm. The corresponding iron(II) complex has torsion angles of this pyridine with the Fe–NCMe axis at 12–15°.

Figure 7 presents a plot of chemical shifts of the pyridine  $\beta$ ,  $\beta'$  and  $\gamma$ -proton shifts versus torsion angles. It is clear that the  $\beta$  protons span the largest range of chemical shifts that are well correlated with torsion angle. A similar relationship is observed for the  $\beta'$  protons, but the slope is not as steep. In contrast, the  $\gamma$  protons, with one exception, are not affected much by a change of torsion angle. Further work is needed to provide a fundamental rationale for the data presented in this figure.

Considering that all of these  $S = 1$  tetragonal oxoiron(IV) complexes have similar electronic configurations in which the unpaired electrons are located on the  $d_{xz}$  and  $d_{yz}$  orbitals, the dramatic differences in  $^1\text{H}$ -NMR chemical shifts for the pyridine ring protons are controlled by the torsion angles between the  $\text{Fe}^{\text{IV}}=\text{O}$  unit and the pyridine plane. Figure 7 shows that there is a linear correlation between the chemical shift of  $\beta$ -H's and the torsion angle. The paramagnetic shifts appear to depend mainly on the torsion angles of the pyridines with the Fe=O unit. In contrast, the  $\gamma$ -H chemical shifts do not show such a large dependence on the torsion angle because they are mainly located on the nodal planes of the  $d_{yz}$  and  $d_{xz}$  orbitals. These orbitals host more than 90% of the unpaired spin density in the whole molecule. More generally, this work demonstrates a method to probe the orientation of chemical bonds and aromatic rings by analyzing the paramagnetic  $^1\text{H}$ -NMR shifts of the pyridine protons.

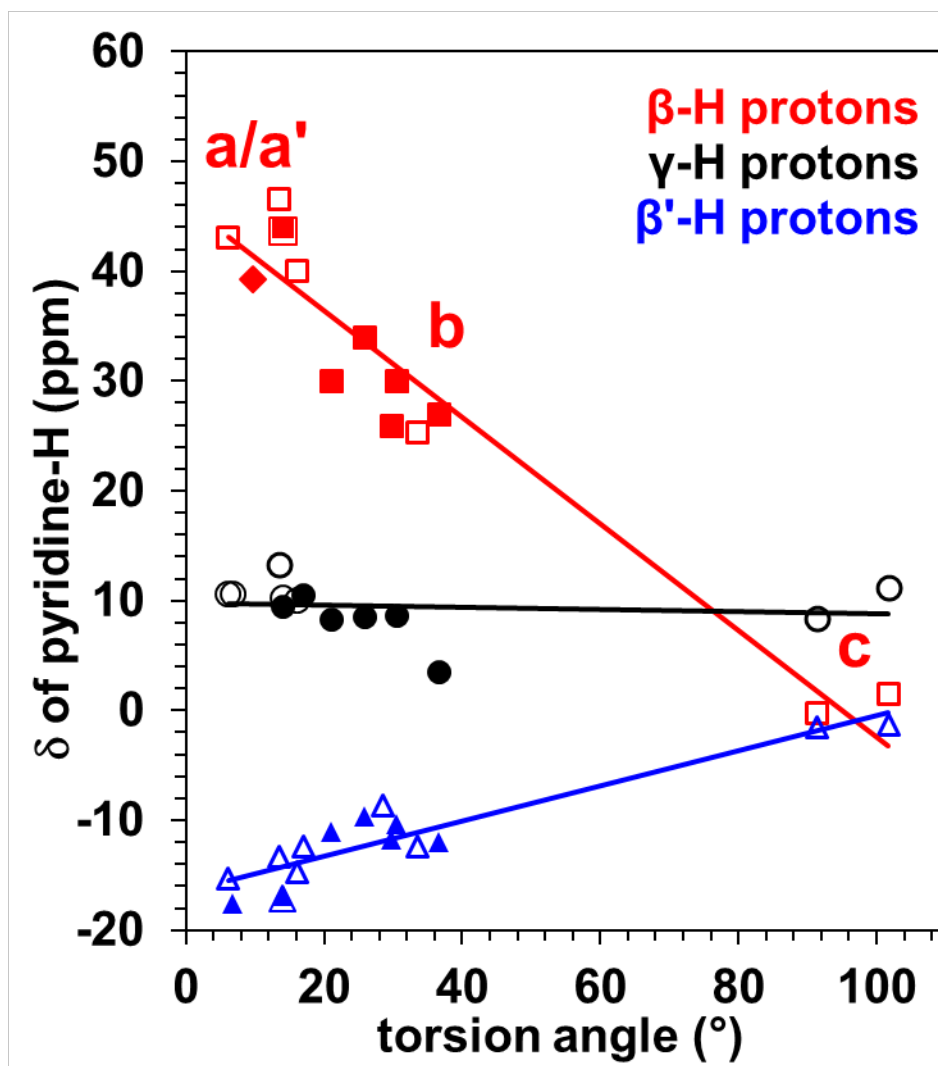


**Figure 7** Correlation between pyridyl proton resonances at 298 K and torsion angles of equatorial pyridines relative to the  $\text{Fe}^{\text{IV}}(\text{O})$  unit or the  $\text{Fe}^{\text{II}}\text{-L}^{6\text{th}}$  bond. Filled shapes correspond to angles obtained from crystallographically characterized oxoiron(IV) complexes **1**, **1-5Me**, **2-B**, **2-Q** and **5**, while open shapes represent angles obtained from the crystal structures of iron(II) precursors of **1-6Me**, **1-6'Me**, **3** and **4**.<sup>46-48, 50</sup> The **a**, **b**, and **c** labels reflect the different orientations of the pyridines relative to the  $\text{Fe}=\text{O}$  unit, as discussed in the text. The solid diamond represents the pyridine **a**  $\beta$ -H from **1-6'ArF<sub>2</sub>** for which the spectrum was obtained at 253 K.<sup>16</sup> See SI for more information.



**Acknowledgments:**

We gratefully acknowledge the support of the U.S. National Science Foundation (grants CHE-1665391 to L.Q. and CHE-1654060 to Y.G.). The Bruker Avance III HD nanobay 400 MHz spectrometer used in this study was purchased from funds provided by the Office of the Vice President of Research, the College of Science and Engineering, and the Department of Chemistry at the University of Minnesota. The Bruker-AXS D8 Venture Diffractometer was purchased through a grant from NSF/MRI 1229400 and the University of Minnesota. We thank Dr. Letitia Yao for her help with NMR experiments and Dr Victor G. Young and Shuangning Xu for their valuable input on X-ray crystallography. We also thank the Pittsburgh Supercomputing Center for granting us computational resources (CHE180020P to R.F. and Y.G.).

**Conflicts of Interest:**

The authors declare no conflict of interest.

**ORCID ID:**

Waqas Rasheed: 0000-0003-3353-9347

Ruixi Fan: 0000-0002-6996-4276

Chase S Abelson: 0000-0001-9919-2855

Paul O Peterson: 0000-0002-0602-2695

Wei Min Ching: 0000-0002-5299-4479

Yisong Guo: 0000-0002-4132-3565

Lawrence Que, Jr: 0000-0002-0989-2813

## References

1. Kal, S.; Que, L., *J. Biol. Inorg. Chem.* **2017**, 22 (2), 339-365.
2. Bollinger Jr, J. M.; Chang, W.-C.; Matthews, M. L.; Martinie, R. J.; Boal, A. K.; Krebs, C., In *2-Oxoglutarate-Dependent Oxygenases*, Hausinger, R. P.; Schofield, C. J., Eds. Royal Society of Chemistry: 2015; pp 95-122.
3. Krebs, C.; Galonić Fujimori, D.; Walsh, C. T.; Bollinger, J. M., *Acc. Chem. Res.* **2007**, 40 (7), 484-492.
4. Sinnecker, S.; Svensen, N.; Barr, E. W.; Ye, S.; Bollinger, J. M.; Neese, F.; Krebs, C., *J. Am. Chem. Soc.* **2007**, 129 (19), 6168-6179.
5. Tamanaha, E.; Zhang, B.; Guo, Y.; Chang, W.-c.; Barr, E. W.; Xing, G.; St. Clair, J.; Ye, S.; Neese, F.; Bollinger, J. M.; Krebs, C., *J. Am. Chem. Soc.* **2016**, 138 (28), 8862-8874.
6. Yu, C.-P.; Tang, Y.; Cha, L.; Milikisiyants, S.; Smirnova, T. I.; Smirnov, A. I.; Guo, Y.; Chang, W.-c., *J. Am. Chem. Soc.* **2018**, 140 (45), 15190-15193.
7. McDonald, A. R.; Que, L., Jr., *Coord. Chem. Rev.* **2013**, 257 (2), 414-428.
8. Klein, J. E. M. N.; Que, L., Biomimetic High-Valent Mononuclear Nonheme Iron-Oxo Chemistry. In *Encyclopedia of Inorganic and Bioinorganic Chemistry*, John Wiley & Sons, Ltd: 2016; p; DOI: 10.1002/9781119951438.eibc2344
9. Engelmann, X.; Monte-Pérez, I.; Ray, K., *Angew. Chem. Int. Ed.* **2016**, 55 (27), 7632-7649.
10. Rohde, J.-U.; In, J.-H.; Lim, M. H.; Brennessel, W. W.; Bukowski, M. R.; Stubna, A.; Münck, E.; Nam, W.; Que, L., *Science* **2003**, 299 (5609), 1037.
11. Thibon, A.; England, J.; Martinho, M.; Young Jr, V. G.; Frisch, J. R.; Guillot, R.; Girerd, J.-J.; Münck, E.; Que Jr, L.; Banse, F., *Angew. Chem. Int. Ed.* **2008**, 47 (37), 7064-7067.
12. England, J.; Bigelow, J. O.; Van Heuvelen, K. M.; Farquhar, E. R.; Martinho, M.; Meier, K. K.; Frisch, J. R.; Münck, E.; Que, L., *Chem. Sci.* **2014**, 5 (3), 1204-1215.
13. Prakash, J.; Rohde, G. T.; Meier, K. K.; Münck, E.; Que, L., *Inorg. Chem.* **2015**, 54 (23), 11055-11057.
14. Schaub, S.; Miska, A.; Becker, J.; Zahn, S.; Mollenhauer, D.; Sakshath, S.; Schünemann, V.; Schindler, S., *Angew. Chem. Int. Ed.* **2018**, 57 (19), 5355-5358.
15. Klinker, E. J.; Kaizer, J.; Brennessel, W. W.; Woodrum, N. L.; Cramer, C. J.; Que, L., Jr., *Angew. Chem. Int. Ed.* **2005**, 44 (24), 3690-3694.
16. Sahu, S.; Zhang, B.; Pollock, C. J.; Dürr, M.; Davies, C. G.; Confer, A. M.; Ivanović-Burmazović, I.; Siegler, M. A.; Jameson, G. N. L.; Krebs, C.; Goldberg, D. P., *J. Am. Chem. Soc.* **2016**, 138 (39), 12791-12802.
17. Rasheed, W.; Draksharapu, A.; Banerjee, S.; Young, V. G.; Fan, R.; Guo, Y.; Ozerov, M.; Nehr Korn, J.; Krzystek, J.; Telser, J.; Que, L., *Angew. Chem. Int. Ed.* **2018**, 57 (30), 9387-9391.
18. Ming, L.-J., Nuclear Magnetic Resonance of Paramagnetic Metal Centers in Proteins and Synthetic Complexes. In *Physical Methods in Bioinorganic Chemistry. Spectroscopy and Magnetism*, Que, L., Jr., Ed. University Science Books: Sausalito, CA: 2000; pp 375-464.
19. Bertini, I.; Luchinat, C.; Parigi, G., *Elsevier* **2001**, *Solution NMR of Paramagnetic Molecules: Applications to Metallobiomolecules and Models*.

20. Nájera, C.; Gil-Moltó, J.; Karlström, S., *Adv. Synth. Catal.* **2004**, 346 (13-15), 1798-1811.
21. Nanthakumar, A.; Fox, S.; Murthy, N. N.; Karlin, K. D., *J. Am. Chem. Soc.* **1997**, 119 (17), 3898-3906.
22. Klinker, E. J., **2007**, University of Minnesota, Minneapolis, MN.
23. Chantarojsiri, T.; Sun, Y.; Long, J. R.; Chang, C. J., *Inorg. Chem.* **2015**, 54 (12), 5879-5887.
24. Bechlars, B.; D'Alessandro, D. M.; Jenkins, D. M.; Iavarone, A. T.; Glover, S. D.; Kubiak, C. P.; Long, J. R., *Nature Chem.* **2010**, 2, 362.
25. Lubben, M.; Meetsma, A.; Wilkinson, E. C.; Feringa, B.; Que Jr, L., *Angew. Chem. Int. Ed.* **1995**, 34 (13-14), 1512-1514.
26. Duelund, L.; Hazell, R.; McKenzie, C. J.; Preuss Nielsen, L.; Toftlund, H., *J. Chem. Soc., Dalton Trans.* **2001**, (2), 152-156.
27. Ching, W.-M.; Zhou, A.; Klein, J. E. M. N.; Fan, R.; Knizia, G.; Cramer, C. J.; Guo, Y.; Que, L., *Inorg. Chem.* **2017**, 56 (18), 11129-11140.
28. Kaizer, J.; Klinker, E. J.; Oh, N. Y.; Rohde, J.-U.; Song, W. J.; Stubna, A.; Kim, J.; Münck, E.; Nam, W.; Que, L., Jr., *J. Am. Chem. Soc.* **2004**, 126 (2), 472-473.
29. APEX3, Bruker Analytical X-ray Systems, Madison, WI (2016).
30. SADABS, Bruker Analytical X-ray Systems, Madison, WI (2016).
31. SAINT, Bruker Analytical X-ray Systems, Madison, WI (2016).
32. SHELXTL, a., Bruker Analytical X-Ray Systems, Madison, WI (2008); b) G. M. Sheldrick, *Acta Cryst. A* **64**, 112-122 (2008).
33. 2016/6, S.; Sheldrick, G. M., *Acta Cryst.* **2015**, (C71), 3-8.
34. Frisch, M. J.; Trucks, G. W.; Schlegel, H. B.; Scuseria, G. E.; Robb, M. A.; Cheeseman, J. R.; Scalmani, G.; Barone, V.; Petersson, G. A.; Nakatsuji, H.; Li, X.; Caricato, M.; Marenich, A. V.; Bloino, J.; Janesko, B. G.; Gomperts, R.; Mennucci, B.; Hratchian, H. P.; Ortiz, J. V.; Izmaylov, A. F.; Sonnenberg, J. L.; Williams-Young, D.; F. Ding, F. L.; Egidi, F.; Goings, J.; Peng, B.; Petrone, A.; Henderson, T.; Ranasinghe, D.; Zakrzewski, V. G.; J. Gao, N. R.; Zheng, G.; Liang, W.; Hada, M.; Ehara, M.; Toyota, K.; Fukuda, R.; Hasegawa, J.; Ishida, M.; Nakajima, T.; Honda, Y.; Kitao, O.; Nakai, H.; Vreven, T.; Throssell, K.; Jr., J. A. M.; Peralta, J. E.; Ogliaro, F.; Bearpark, M. J.; Heyd, J. J.; Brothers, E. N.; Kudin, K. N.; Staroverov, V. N.; Keith, T. A.; Kobayashi, R.; Normand, J.; Raghavachari, K.; Rendell, A. P.; Burant, J. C.; Iyengar, S. S.; Tomasi, J.; Cossi, M.; Millam, J. M.; Klene, M.; Adamo, C.; Cammi, R.; Ochterski, J. W.; Martin, R. L.; Morokuma, K.; Farkas, O.; Foresman, J. B.; Fox, D. J., *Gaussian, Inc., Wallingford CT*, 2016.
35. Borgogno, A.; Rastrelli, F.; Bagno, A., *Chem. Eur. J.* **2015**, 21 (37), 12960-12970.
36. Borgogno, A.; Rastrelli, F.; Bagno, A., *Dalton Trans.* **2014**, 43 (25), 9486-9496.
37. Rastrelli, F.; Bagno, A., *Magn. Reson. Chem.* **2010**, 48 (S1), S132-S141.
38. Rastrelli, F.; Bagno, A., *Chem. Eur. J* **2009**, 15 (32), 7990-8004.
39. Reiher, M., *Inorg. Chem.* **2002**, 41 (25), 6928-6935.
40. Bertini, I.; Luchinat, C.; Parigi, G., *Prog. Nucl. Magn. Reson. Spectrosc.* **2002**, 40 (3), 249-273.
41. Hrobárik, P.; Reviakine, R.; Arbuznikov, A. V.; Malkina, O. L.; Malkin, V. G.; Köhler, F. H.; Kaupp, M., *J. Chem. Phys.* **2007**, 126 (2), 024107.

42. Banerjee, S.; Rasheed, W.; Fan, R.; Draksharapu, A.; Oloo, W. N.; Guo, Y.; Que Jr, L., *Chem. Eur. J.* **2019**, <http://dx.doi.org/10.1002/chem.201902048>.
43. Mukherjee, G.; Lee, C. W. Z.; Nag, S. S.; Alili, A.; Cantú Reinhard, F. G.; Kumar, D.; Sastri, C. V.; de Visser, S. P., *Dalton Trans.* **2018**, 47 (42), 14945-14957.
44. Draksharapu, A.; Angelone, D.; Quesne, M. G.; Padamati, S. K.; Gómez, L.; Hage, R.; Costas, M.; Browne, W. R.; de Visser, S. P., *Angew. Chem. Int. Ed.* **2015**, 54 (14), 4357-4361.
45. Rana, S.; Dey, A.; Maiti, D., *Chem. Commun.* **2015**, 51 (77), 14469-14472.
46. Mukherjee, G.; Alili, A.; Barman, P.; Kumar, D.; Sastri, C. V.; de Visser, S. P., *Chem. Eur. J.* **2019**, 25 (19), 5086-5098.
47. Singh, R.; Ganguly, G.; Malinkin, S. O.; Demeshko, S.; Meyer, F.; Nordlander, E.; Paine, T. K., *Inorg. Chem.* **2019**.
48. Ortega-Villar, N.; Ugalde-Saldívar, V. M.; Muñoz, M. C.; Ortiz-Frade, L. A.; Alvarado-Rodríguez, J. G.; Real, J. A.; Moreno-Esparza, R., *Inorg. Chem.* **2007**, 46 (18), 7285-7293.
49. Company, A.; Sabenya, G.; González-Béjar, M.; Gómez, L.; Clémancey, M.; Blondin, G.; Jasniewski, A. J.; Puri, M.; Browne, W. R.; Latour, J.-M.; Que, L.; Costas, M.; Pérez-Prieto, J.; Lloret-Fillol, J., *J. Am. Chem. Soc.* **2014**, 136 (12), 4624-4633.
50. Spek, A. L.; Schoondergang, M. F. J.; Feringa, B. L., *CSD Communication* **2004**, CCDC 232796.